Electrochimica Acta 56 (2011) 7955–7962

Contents lists available at ScienceDirect

Electrochimica Acta

journal homepage: www.elsevier.com/locate/electacta

Impedance spectroscopy studies of dual membrane fuel cell

Daria Vladikova[a,*,1], Zdravko Stoynov[a,1], Gergana Raikova[a], Alain Thorel[b], Anthony Chesnaud[b], Joao Abreu[b], Massimo Viviani[c], Antonio Barbucci[d], Sabrina Presto[c], Paola Carpanese[d]

[a] Institute of Electrochemistry and Energy Systems – BAS, 10 Acad. G. Bonchev, 1113 Sofia, Bulgaria
[b] Centre des Matériaux, Mines-ParisTech, BP87, Evry Cedex 91003, France
[c] Institute for Energetics and Interphases, CNR, Via De Marini 6, 16149 Genova, Italy
[d] DICheP, University of Genova, P.le Kennedy 1, 16129 Genova, Italy

ARTICLE INFO

Article history:
Received 1 July 2010
Received in revised form 31 January 2011
Accepted 2 February 2011
Available online 18 February 2011

Keywords:
Impedance spectroscopy
Dual membrane fuel cell
Porous oxygen ion and proton conducting membrane
Differential impedance analysis
Water vapor formation

ABSTRACT

This paper reports impedance studies of a dual membrane fuel cell - an innovative design based on the idea for a junction between an oxygen ion conducting cathode/electrolyte part and proton conducting anode/electrolyte part through a mixed oxygen ion and proton conducting porous membrane. Thus oxygen, hydrogen and water are located in three independent chambers. This concept allows avoiding all the severe pitfalls connected to the presence of water at electrodes in both SOFC and PCFC. The performed measurements of the 3 compartments and the data analysis are improved by introducing some specialized approaches and techniques, which are discussed. The impedance contribution in the proof of the new concept is also presented.

1. Introduction

Commercialization of high temperature fuel cells requires decrease of the costs, combined with better performance stability and higher fuel efficiency. The main pathway for realization of these objectives is the reduction of the operation temperature. This target needs improvements of the materials toward lower electrodes polarization resistance and higher electrolyte conductivity, as well as innovations in the cell concept and design. One direction is the optimization of the planar SOFC design and reduction of the active layers thickness. However, this design has one principal disadvantage, which automatically decreases the electrical efficiency - the dilution of the fuel with the water, evacuated through the anode as exhaust product. An improvement in that direction is the development of the proton conducting fuel cell (PCFC), where the more mobile protons are transported through the electrolyte, which reduces the operating temperature. In this design the water is evacuated through the cathode and thus it dilutes the oxygen. Recently an innovative concept for dual membrane fuel cell was introduced [1–3]. It combines the advantages and bypasses the disadvantages of both SOFC and PCFC in respect to the effect of the water. The concept is based on a junction between a SOFC cathode/electrolyte part and PCFC electrolyte/anode part through a mixed oxygen ion and proton conducting porous ceramic membrane. Oxygen ions created at the cathode side progress toward the central membrane where they meet the protons created at the anode side, and produce water, which is evacuated through the interconnecting porous media. In this way oxygen, hydrogen and water are located in 3 independent chambers. The most important advantages of the new design are that: (i) the fuel and the oxygen are not diluted; (ii) water does not inhibit the catalytic activity of the electrodes; (iii) no gas counterflow is needed to sweep water away from electrodes; (iv) every element of the cell has a single role, and therefore can be fully optimized for a single purpose. There are also additional possibilities for increase of the reaction velocity in the central membrane based on the principle of le Chatellier. The dual membrane fuel cell concept is patented [4] and is under development in a FP7 European project [1]. For short it is named “IDEAL-Cell” after the acronym of the project.

Impedance spectroscopy is the main tool applied for testing of the new design. This paper aims at presenting its application for

* Corresponding author. Tel.: +359 2 9714733; fax: +359 2 8722544.
E-mail address: d.vladikova@bas.bg (D. Vladikova).
[1] ISE member.

0013-4686/$ – see front matter © 2011 Elsevier Ltd. All rights reserved.
doi:10.1016/j.electacta.2011.02.007

characterization of the 3 compartments and for the proof of the concept. Some approaches for improvement of the data quality and analysis are also discussed.

2. Experimental

2.1. Materials, cells, experimental conditions

For investigations of the dual membrane fuel cell and its three compartments, the following materials were selected: LSCF48 ($La_{0.6}Sr_{0.4}Co_{0.2}Fe_{0.8}O_{3-\delta}$) as cathode, YDC15 ($Ce_{0.85}Y_{0.15}O_{1.925}$) as oxygen ion conductor; BCY15 ($BaCe_{0.85}Y_{0.15}O_{2-\delta}$) as proton conductor and BCY15-Ni cermet as anode. The initial ceramic powders were produced by Marion Technologies. For elimination the influence of the electrodes quality on the electrolytes characterization, metal (Me = Pt, Ag) electrodes were also used. The impedance measurements were performed on 3 types of symmetrical half cells: electrolyte supported LSCF48/YDC15/LSCF48, electrolyte supported BCY15-Ni/BCY15/BCY15-Ni and central membrane (CM) supported Me/$YDC15_{porous}$$BCY15_{porous}$/Me.

The electrolyte pellets (diameter/thickness = 20–25/1–1,3 mm), including the CM, were prepared by cold pressing and sintering. The ceramic electrodes (thickness 20–30 μm) were deposited on both sides of the support by tape casting (TC) and plasma spraying (PS). The Pt (Metalor) and Ag (Baltic Präparation) electrodes were painted onto both sides of the samples. The Pt layers were sintered in air following a procedure recommended by the producer.

Obviously the most important and innovative part is the central membrane, which consists of 3 phases: BCY15, YDC15 and pores. For a first time a requirement for porous composite electrolyte structure is under study. The design of the CM half cell and the performance of measurements in both air and hydrogen ensured important information about the individual conductivity of every one of the two electrolytes in the presence of the second electrolyte and pores, i.e. in the real structure. The obtained results, however, do not give information about the influence of the water vapor formation and evacuation. For this purpose water vapor permeability tests are under development.

The IDEAL-Cell concept was proved on model BCY15-electrolyte supported cell with diameter 20 mm produced by co-pressing and co-sintering of the three conducting layers assembly and additional deposition of the Pt electrodes: Pt/YDC15 (30 μm)/$(YDC15 + BCY15)_{porous}$ (50 μm)/BCY15 (600 μm)/Pt (Fig. 1). For decreasing the difference of sintering behavior between BCY15 and YDC15 materials, 2 wt.% ZnO was added to BCY15. For the CM, corn starch was used as a pore former.

The impedance measurements were performed on Solartron 1260 FRA in temperature interval 100–750 °C and frequency range from 1 MHz down to 0.01 Hz with density 5 points/decade and different mode and amplitudes of the AC signal. The half cell measurements were carried out at OCV in working atmosphere air (30 N mL/min) or wet (3% H_2O) hydrogen (30 N mL/min). The "proof of concept" (PoC) cell impedance studies were performed in a two-compartment cell rig with isolated hydrogen chamber and a common oxygen and CM space. The measurements were carried out at OCV and under load in optimal in respect to the OCV working atmosphere: air (30 N mL/min) for the cathode side and wet (3% H_2O) hydrogen (15 N mL/min) for the anode side.

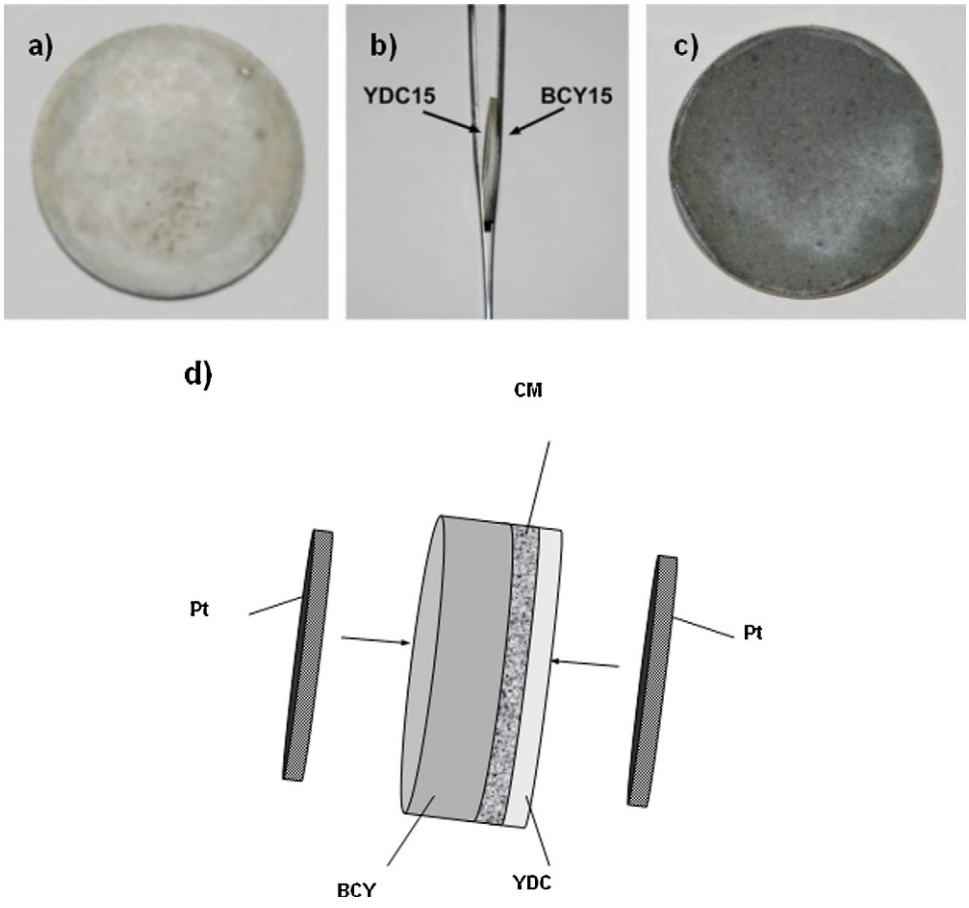

Fig. 1. Proof of concept (PoC) cell: assembly of the three electrolyte layers YDC15/CM/BCY15 produced by co-pressing and co-sintering: (a) YDC15 side, (b) crosswise, (c) BCY15 side; (d) schematic presentation of the cell.

2.2. Approaches for data quality improvement

From electrochemical point of view high temperature fuel cells behave as large statistical systems with distributed parameters in macro- and micro-scale. During experimentation, different processes take place and change their behavior and parameters, which introduces some specific problems. Obviously for improving the accuracy and reliability of the impedance measurements and their analysis, introduction of some specialized approaches and techniques is desirable.

For characterization of both electrolytes and electrodes, the measurements of the half cells were performed in a large temperature interval. The lower temperatures ensure information about the electrolyte behavior, including separation of the bulk from the grain boundaries contribution, while at higher temperatures the electrode reaction is well pronounced. In this large temperature range, the samples' impedance changes from hundreds of megaohms down to milliohms. In order to acquire as much information as possible the frequency range should be also large – from 10 MHz down to 10 and even 1 mHz. According to our experience, the best quality of the experimental data can be ensured by application of two modes of operation – at low temperatures the measurements are performed at potentiostatic conditions with perturbing signal 200–20 mV, obeying the requirement for linearity. At high temperatures, where the sample's impedance is low, the optimal mode is galvanostatic. The sample rig was carefully tested and calibrated in the full temperature, frequency and impedance ranges. As a result, the switch from potentiostatic to galvanostatic mode was carried out at temperatures, when the sample's impedance (the maximum of the modulus) becomes less then 20–10 Ohms. This algorithm ensures best quality of the measured data, covering frequency range which is larger than the conventional. The measurements were performed in a specially constructed furnace with DC power supply and galvanostatic mode of thermal regulation, giving less then 0.6 °C temperature gradient during the measurement (about 3–5 min). The application of this furnace improves the quality of the impedance measurements, eliminating the production of erroneous data at frequencies near to the power supply frequency, as well as to its harmonics – 50, 100, 150, 250 Hz.

Another specific problem that complicates the measurements is the low impedance of the sample at high operating temperatures, which increases the influence of the cell rig parasitic inductance and resistance and usually decreases the accuracy of the electrolyte resistance evaluation. For this purpose a new 4 wires testing rig (4 wires, 2 points) was developed and an improved procedure for parasitic inductance and resistance correction based on previously developed algorithm [5–7] was introduced. The calibration of the testing rig (short circuit measurements) was performed at room and elevated temperatures in the full temperature and frequency range. The correction procedure improved the accuracy in the determination of the electrolyte resistance at 700 °C with about 30% (Fig. 2).

2.3. Approaches for improvement of data analysis

From impedance point of view fuel cells are "fuzzy" objects with strong, unpredictable distribution of the parameters. The existing models for description of their behavior are exception rather than a rule. In this study the technique of the differential impedance analysis (DIA), described in details in [5,7–9], was applied. It extracts the model structure directly from the experimental data without using a preliminary working hypothesis.

In short DIA performs a local parametric analysis by a Local Operating Model (LOM) moving along the frequency [5,7,8]. Its structure consists of: additive resistance r_{ad}, connected in series with a single mesh of R and capacitance C connected in parallel. In addition the effective time-constant $T = RC$ is introduced as a parameter. The identification of the LOM parameters estimates $\hat{P}_{LOM}$ for every experimental point converts the initial experimental data set $D_1 = [\omega_i, Z'_i, Z''_i]$ into a new, estimated one $D_2[\log\omega_i, \log\hat{r}_{adi}, \log\hat{C}_i, \log\hat{R}_i, \log\hat{T}_i]$. The temporal analysis of their vector $\hat{P}_{LOM}$ follows the relationship:

$$\log\hat{P}_{LOMi} = F(\log\omega^{-1}) = F\left(\log\frac{T_f}{2\pi}\right) \quad (1)$$

where $T_f = 1/f$ and f is the frequency.This analysis is very convenient for recognition of processes described with time-constants and ensures both structural and parametric identification with high selectivity. The temporal plots represent in an illustrative form the model structure. The presence of plateaus recognizes time constant sub-models, while their position enables the estimation of the parameters (Fig. 3a and b).

When the LOM does not correspond to the object's structure, the parameters estimates are frequency dependent. This behavior can be identified by differentiation of the temporal dependencies (secondary DIA):

$$\hat{\delta}_{\hat{P}_{LOM}} = \frac{d\log\hat{P}_{LOM}}{d\log\omega} = \Phi(\log\omega^{-1}) = \Phi\left(\log\frac{T_f}{2\pi}\right) \quad (2)$$

The procedure is described in more details in [5,9]. DIA has been successfully applied for studies of composite LSM/YSZ cathodes and YSZ electrolyte based on the $\hat{R}$-temporal analysis [10–13]. In this study we performed temporal and differential temporal analysis of $\hat{r}_{ad}$ and $\hat{R}$ for better separation of the bulk from the grain boundaries electrolyte resistance.

The temporal analysis of $\hat{r}_{ad}$ ensures identification of the phenomena preceding the one identified by the parameter $\hat{R}$. The results on simulated data presented in Fig. 3 illustrate the high selectivity, which ensures recognition of the resistance for the invisible in the Z-plot phenomena by $\hat{r}_{ad}$ in cases when the arc corresponding to the first visible process (recognized by $\hat{R}$) is partially observable. It should be emphasized that the analysis is working with very high selectivity for processes well described with lumped time-constants. In real systems, where frequency distribution is usually observed, the selectivity decreases.

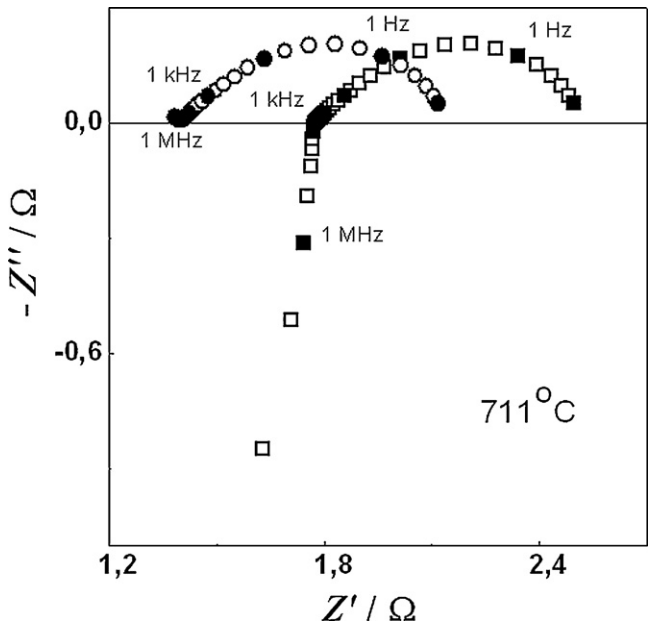

Fig. 2. Complex plane impedance diagram of cathodic symmetrical half cell before (□) and after (○) the parasitic rig inductance and resistance correction.

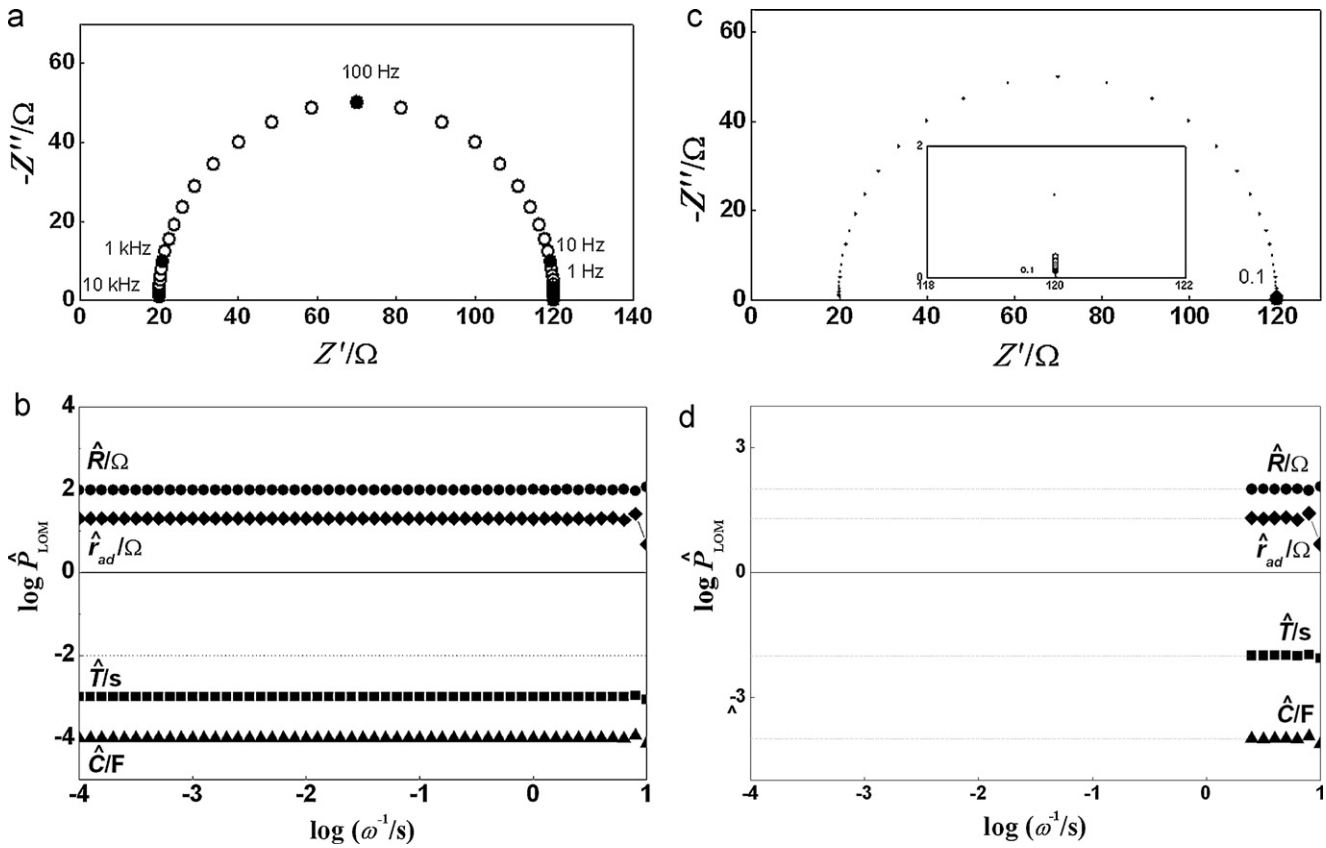

Fig. 3. DIA of simulated time-constant model with additive resistance: (a) complex plane impedance diagram simulated in angular frequency range 10^4–10^{-1} s^{-1}; (b) corresponding temporal plot; (c) the same model simulated in angular frequency range 0.31–0.10 s^{-1}; (d) corresponding temporal plot.

3. Results and discussion

3.1. DIA of symmetrical half cells

The impedance characterization of the cell compartments was performed on the 3 types of half cell samples described in the previous section. Due to the correction of the cell rig parasitic components, at elevated temperatures a capacitive arc corresponding to the grain boundary contribution replaces the typical high frequency inductive tail (Figs. 2 and 4a). The combined $\hat{R}$ and $\hat{r}_{ad}$ temporal analysis ensured improved estimation of the bulk and grain boundary resistance and respectively of the total resistance. As presented in Fig. 4b, the grain boundaries contribution of the oxygen ion conducting electrolyte (R_{gb}) can be estimated by the corresponding plateau in the $\hat{R}$-temporal plot. The contribution of the bulk (R_b) is invisible in this plot, but the first plateau in the $\hat{r}_{ad}$ temporal plot recognizes the bulk resistance, which is an additive term in respect to the grain boundaries resistance. The application of this procedure increased the temperature range for separation of the bulk and grain boundary resistivities of the oxygen conducting electrolyte. Their temperature dependence, which can be observed in the corresponding Arrhenius plots (Fig. 5), give indirect information about the topology of the grain boundaries [14]. The activation energies of the grains interior and grain boundaries are similar which is an indication for the formation of grain boundaries clean of continuous grain boundary phase. The small resistance of the grain boundaries could be explained by enhanced defect concentration in the space charge region [14–17]. The DIA procedure increased also the accuracy of the electrolytes conductivity characterization in the other two compartments (hydrogen compartment and CM). The Arrhenius plots summarize the obtained results (Fig. 6).

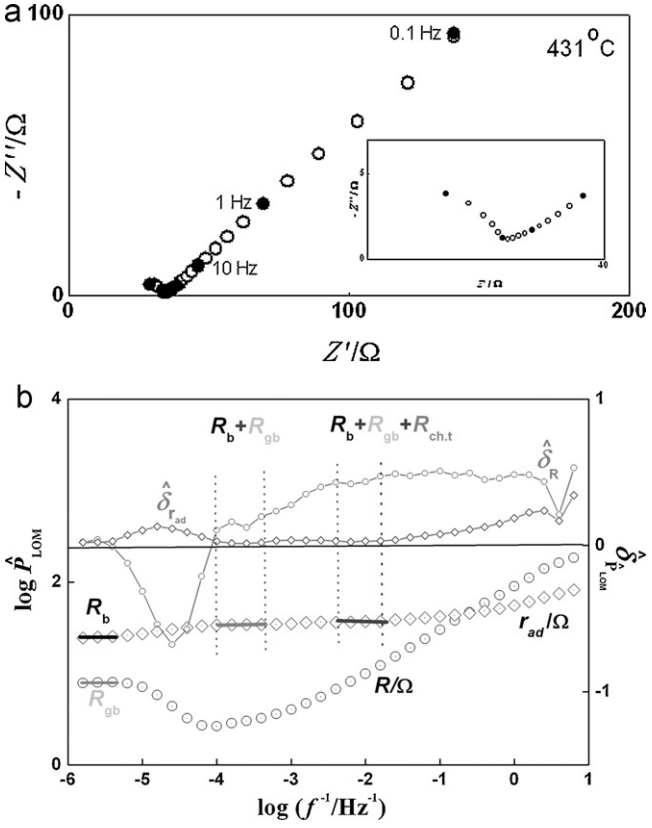

Fig. 4. Cathodic symmetrical half cell: (a) complex plane impedance diagram, (b) corresponding $\hat{r}_{ad}$- and $\hat{R}$-temporal plots and $\hat{\delta}_{r_{ad}}$ and $\hat{\delta}_R$ differential temporal plots.

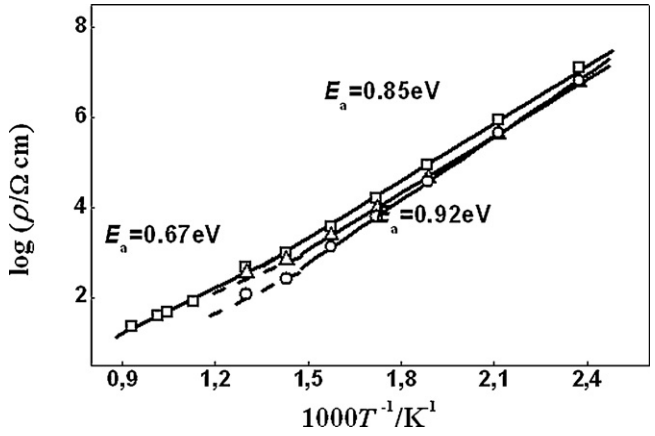

Fig. 5. Arrhenius plots for the bulk (△), grain boundary (○) and total (□) resistivity of YDC15. (The resistivities are calculated with respect to the electrolyte pellet geometry).

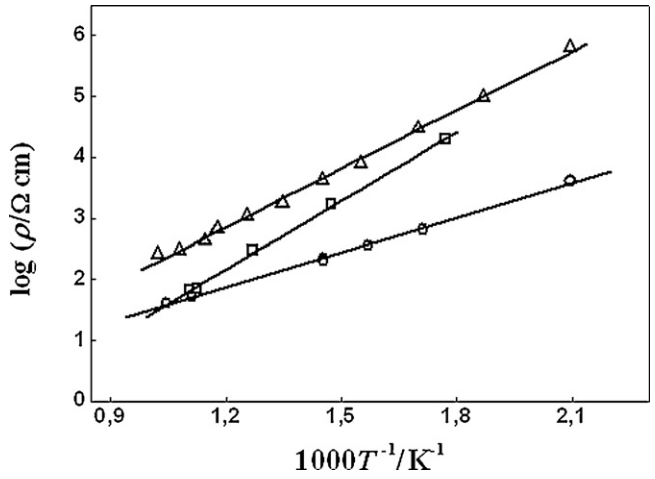

Fig. 6. Arrhenius plots for the total resistivity of: dense BCY15 (○), BCY15 in the porous CM (□), YDC15 in the porous CM (△).

The DIA technique was applied also for deeper insight into the mechanism of the cathode reduction, which gives big contribution to the resistivity of the dual cell. It was found that the LSCF electrodes deposited by tape casting and plasma spraying follow the same reaction mechanism, although exhibiting differences in the impedance shape (Fig. 7). Two steps were recognized: charge transfer at higher frequencies, followed by the rate limiting step, which is frequency dependent and represents the transport limitations of the charged species in the bulk. However, significant parametric differences were registered. For the sample prepared by TC the charge transfer is very fast and its contribution in the polarization resistance is negligible, while for the plasma spray deposition the charge transfer contribution at 600–700 °C is 30–40% from the total polarization resistance (Fig. 8).

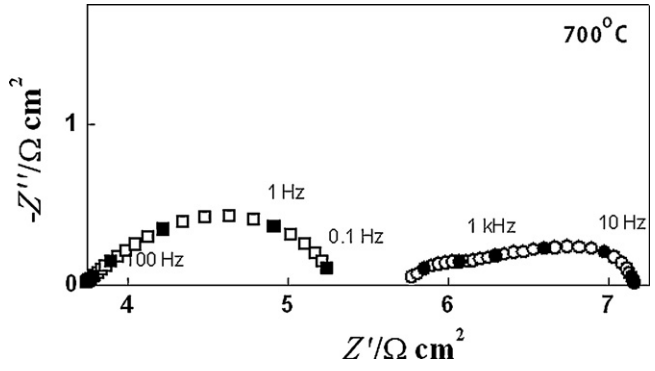

Fig. 7. Complex plane impedance diagrams of cathodic symmetrical half cells with electrodes deposited by: (□) tape casting and (○) plasma spraying.

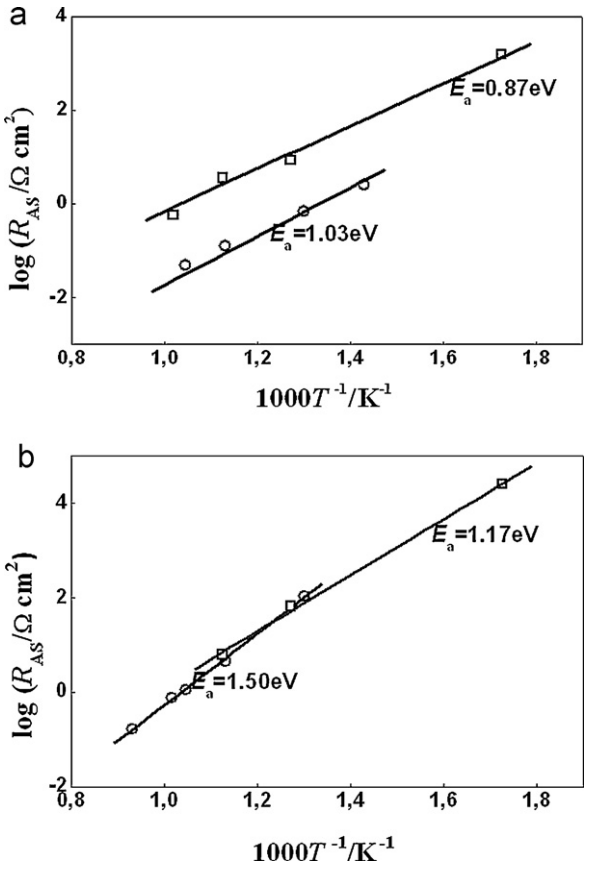

Fig. 8. Cathode reaction behavior: (a) Arrhenius plots of the charge transfer Area Specific Resistance ($R_{AS}/\Omega\,cm^2$) for TC deposition (○) and PS deposition (□); (b) Arrhenius plots of the transport (BCP) Area Specific Resistance ($R_{AS}/\Omega\,cm^2$) for TC deposition (○) and PS deposition (□), estimated by the BCP parameter R_0.

For the electrodes deposited by TC the $\hat{R}$-temporal plot is not sensitive to the charge transfer step (Fig. 4b). The $\hat{r}_{ad}$-temporal analysis has higher selectivity, which, however, decreases when frequency distribution is observed. The two characteristic segments determining $R_b + R_{gb.}$ and $R_b + R_{gb} + R_{ch.t}$ were defined combining the $\hat{r}_{ad}$-temporal analysis (Eq. (1)) with the $\delta_{r_{ad}}$-differential temporal analysis (Eq. (2)) as a supporting tool, since the value of the derivative $\hat{\delta}_{r_{ad}}$ is 0 in the plateau regions of the temporal plot (Fig. 4b). This approach was used for estimation of the charge transfer step down to values of about 60–100 mΩ. It needs further improvement for analysis in the presence of frequency dependent phenomena, which will improve the selectivity.

The second low frequency step is described with diffusion of CPE character ($n \sim 0.5$) in the temperature range 300–500 °C. Above that temperature the acceleration of the oxygen ions transportation brings to bounded conditions, which follow the model of bounded constant phase element (BCP). It represents the impedance of a bounded homogeneous layer with CPE behavior of the conductivity in the elementary volume and a finite conductivity at DC [5]:

$$Z_{BCP}(i\omega) = A^{-1}(i\omega)^{-n} \tan hR_0A(i\omega)^n \quad (3)$$

where A, n and R_0 are the structural parameters of the element. More information about BCP and its DIA identification is given in [5,9,11].

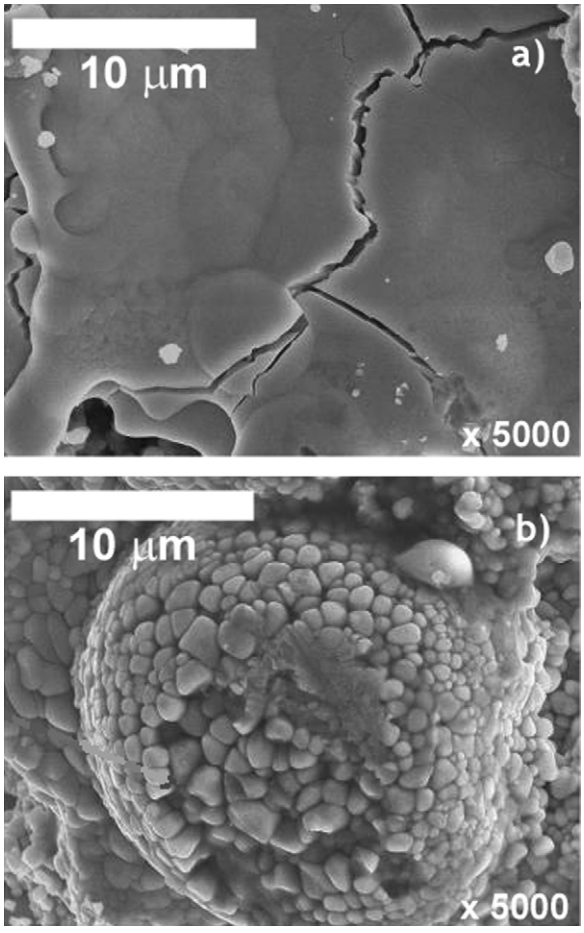

Fig. 9. SEM images of different microstructures on plasma sprayed cathode surface: (a) region with melted splats; (b) region with non-molten granulates.

For the TC sample the exponential coefficient n keeps value close to 0.5 up to 500–550 °C and then decreases. The physical meaning of $n < 0.4$ corresponds to transport limitation of species (oxygen ions) due to restrictions in the host matrix. For the PS deposited electrodes the BCP arc is more depressed (Fig. 7) and n is about 2 times smaller which should be related to a larger inhomogeneity, confirmed by SEM analysis (Fig. 9). The Arrhenius plots of the low frequency step for the LSCF48 electrodes deposited by TC and SP are represented in Fig. 8b.

Since the rate limiting stage in the oxygen reduction reaction is related to transport limitation of the oxygen ions in the electrode matrix, the introduction of a composite cathode material is a possible solution for improved performance.

3.2. Impedance contribution in the proof of the dual membrane fuel cell concept

The proof of the innovative dual membrane fuel cell concept is a key moment for its further development. The following four criteria have been chosen and successfully experimentally confirmed on the "proof of concept" (PoC) cell [1,2]:

- A stable OCV under hydrogen and air at 600 °C;
- A stable polarization V/I curve;
- A specific impedance fingerprint giving evidence for the production of water;
- Direct measurement of water production in the central membrane during current flow through the cell.

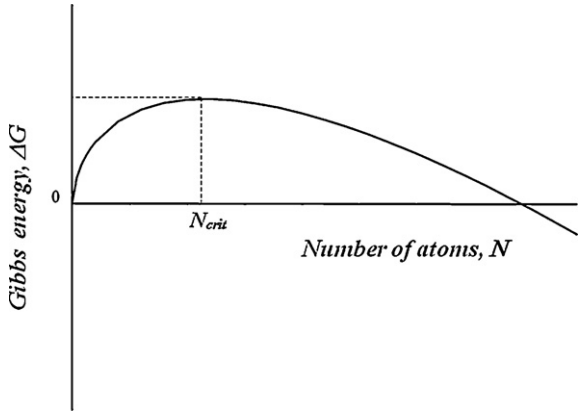

Fig. 10. Gibbs energy of cluster formation.

In this paper the impedance fingerprint of the water formation is discussed.

The theoretical background for the search of impedance fingerprint for water production in the CM can be found in the classical Gibbs theory for formation and growth of new phases (Fig. 10) [18]. When the clusters of the new phase are small, i.e. under the critical size, their growth needs additional energy. From impedance point of view the differential resistance is positive. When the clusters reach the critical size, their further growth becomes a spontaneous process, i.e. they continue to grow with smaller external chemical potential. This process corresponds to "negative" differential resistance in the impedance diagrams. Its mathematical description is introduced in [19] on a two-step reaction model. When the reaction rate coefficient of the low frequency (second) step is higher than that of the first step, the impedance diagram has an inductive loop. This behavior is experimentally observed in electro-crystallization of metals, in new phase formation at the electrodes of classical lead-acid batteries, in corrosion and others [19–21].

The challenge in the notification of impedance fingerprint, i.e. of an inductive loop, is to find experimental conditions in which the water vapor formation in the porous CM during cell operation would become an observable phenomenon. Since IDEAL-Cell is an innovative and complicated impedance object, it is expected that there will be a bigger number of processes in comparison to those observed in a classical SOFC, some of them not studied or even described. Additional deformations in the impedance diagrams, due to increased inhomogeneity, are expected. The large number of phenomena distributed in a frequency range of 6–8 decades brings to a stronger overlapping. However, the rate limiting steps, which should be pronounced better, are of importance. The most challenging is the impedance behavior of the CM, where in addition to the hopping of oxygen ions and protons in the two porous electrolytes, water vapor formation and growth, transport (diffusion) in the pores and evacuation out of the CM occurs. The picture is additionally complicated due to the unknown pores geometry and size (cylindrical geometry could be only a first approximation), the hydrophilic properties of BCY15, the defect structure of the pore walls (with supposed depletion zones, adsorption and surface diffusion of charged species) etc.

The impedance measurements of the model dual membrane fuel cell during operation at optimized wet hydrogen and oxygen flows were performed at different working points determined by the temperature (500 °C and 600 °C) and the current load. Two typical impedance shapes were obtained (Fig. 11). The expected inductive loop (Fig. 11a) appears when the measurement is performed at low load after OCV, while at big load it is replaced with the so called "turtle tail" (Fig. 11b). Obviously the impedance notification for water formation needs special selection of the working point.

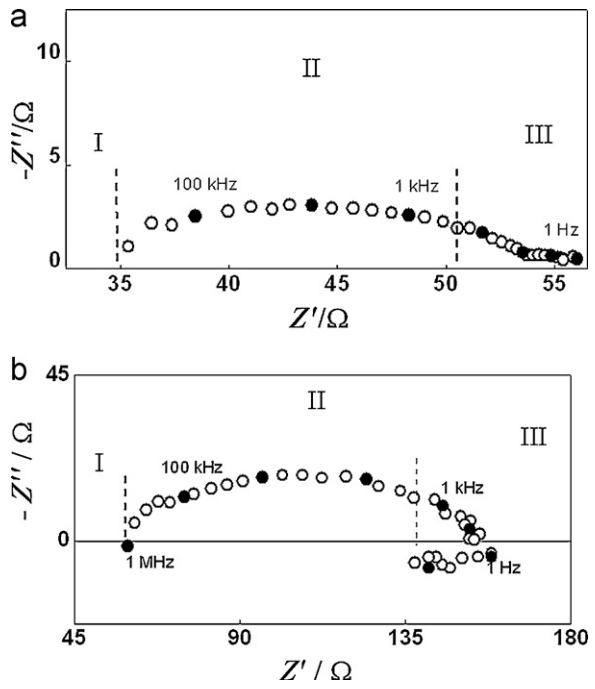

Fig. 11. Complex plane impedance diagrams of PoC cell at 600 °C: (a) measurements at small load after OCV (AC = 0.5 mA, DC = 2 mA); (b) measurements at bigger load (AC = 0.5 mA, DC = 8 mA). (Segments I, II, and III define three zones of the impedance diagrams which are discussed in the text.)

For initial recognition of the impedance diagrams they were compared with the diagrams of the anode, cathode and CM compartments obtained on half-cells. The intercept with the real part of the dual cell impedance diagrams gives the resistances of the two electrolytes and the central membrane (Fig. 11 - segment I). Part of the depressed capacitive arc, where at least three phenomena are overlapping, is related to the polarization of the two electrodes (Fig. 11 - segment II). The lowest frequency segment III which has behavior differing from that of segment II should be attributed to the water vapor formation and transport. The segmentation is done with the help of DIA. On this stage more detailed DIA analysis is not performed.

For interpretation of the experimental results the following working hypothesis was proposed. The formation of the water molecules at the triple phase boundary BCY15/YDC15/pore by reaction of the most active particles – protons and oxygen ions, is expected to be a fast process (when it occurs). However, a certain threshold should be overcome. Very probably the water vapor molecules do not have the behavior of single particles (molecules), but form clusters, since this configuration is more stable, especially in the supposed conditions in the pores - defect structure of the two electrolytes, hydrophilic properties of the BCY etc.

The transport of the produced species – water molecules or partially charged water-based species in the pores is expected to be visible in the lowest frequency part of the impedance diagrams. It may follow different mechanisms – surface diffusion, volume diffusion or both. The defect structure of the electrolytes and the hydrophilic properties of the BCY are in favor of adsorption or surface semi-liquid layer formation. At low current, (small load) a smaller number of water vapor clusters will be formed. They are separated and their growth before overlapping can be observed. In that case the water formation/growth will be registered by impedance as negative resistance. If the current is high (big load), a big number of clusters will be formed. They will easily overlap and the effect of the growth will be fast and invisible from impedance point of view. In this case, however, the transport in the pores, eventually with/through the quasi liquid film, will be observed. The physical meaning of the "turtle tail" concerns transport limitations of species that do not change their state. Such behavior was noticed in Li-ion cells intercalation studies [22].

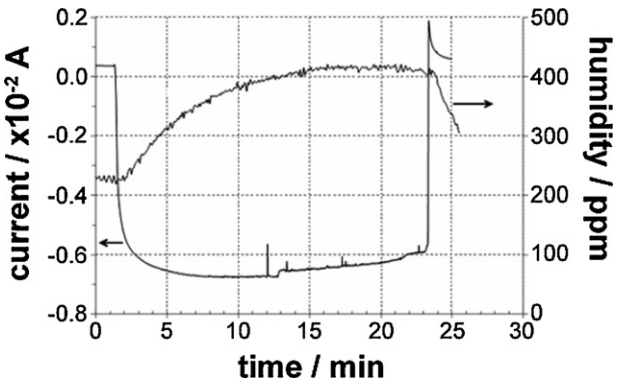

Fig. 12. Registration of water formation in the central membrane of the PoC cell operating at pulsed load potential.

As a conclusion, the observed inductive loop in the impedance diagrams can be regarded as a fingerprint for the water vapor formation and can be added to the other strong evidences for the proof of the concept.

For the direct measurement of water formation in the central membrane, a new cell rig (PoC tester) was developed, where the three compartments were fully separated. This construction ensures conditions for quantitative measurement of the water produced in the central membrane from the recombination of oxygen and hydrogen ions. The central membrane was connected with a moisture analyzer (Microview, Manalytical, UK). Nitrogen flow was used to transport the water form the CM to the analyzer. The measurements were performed in a regime of pulsed load potential. The result presented in Fig. 12 shows a sharp increase of the humidity in the third chamber at current flow. When the potentiostatic polarization is stopped, the humidity goes down. The registered bias level of humidity before the polarization could be due to the nitrogen flow through the system, to possible tiny leakage, to adsorption of water in the CM and the connecting pipes. More detailed description of the experimental results for the direct measurement of the water evacuation from the CM is in preparation.

4. Conclusions

The performed impedance studies of the innovative dual membrane fuel cell support the proof of the concept and the experimental directions for its further optimization. The evaluation of the electrolytes resistivity in the tree compartments obtained by the symmetric half cells measurements is found to be 3–4 times smaller than that measured on the model cell, where water is produced in the CM. The results show that the water evacuation is an important step for the cell optimization. There are two challenges: (i) "electrical" optimization, which aims at increasing the CM conductivity by improving composition, microstructure, volume fraction of the two electrolytes, geometry of the CM and (ii) "physical" optimization, where the main target is the porosity with regard to the water vapor evacuation. One solution could be the presence of double porous structure with additional bigger collector channels for the water vapor evacuation. A promising experimental approach is the combination of water vapor permeability studies with tortuosity measurements of the two ions hopping pathways performed by impedance spectroscopy.

Acknowledgements

The research leading to these results has received funding from the European Community's Seventh Framework Programme (FP7/2007-2013) under grant agreement No 213389. Powders were fabricated and supplied by Marion Technologies. Plasma sprayed deposition was performed at DLR.

Appendix A. Nomenclature

A	proportional coefficient of CPE (Ω^{-1} s^n)
AC	alternative current (A)
R_{SR}	area specific resistance (Ω^{-1} s^n)
BCP	bounded constant phase element
BCY15	$BaCe_{0.85}Y_{0.15}O_{2-\delta}$
C	capacitance ($F = s\,\Omega^{-1}$)
$\hat{C}_i$	estimate of the capacitance ($F = s\,\Omega^{-1}$)
CM	central membrane
CPE	constant phase element
DC	direct current (A)
DIA	differential impedance analysis
f	frequency (Hz)
F	function
I	current (A)
L	inductance ($H = \Omega\,s$)
LOM	local operating model
LSCF48	$La_{0.6}Sr_{0.4}Co_{0.2}Fe_{0.8}O_{3-\delta}$
n	exponential factor of CPE
N	number of atoms
N_{crit}	critical number of atoms
OCV	open circuitry voltage
$\hat{P}_{LOM}$	numerical vector of the LOM parameters
PCFC	proton conducting fuel cell
PoC	proof of concept
ppm	parts-per-million (in this study volume parts)
R	resistance (Ω)
$\hat{R}$	estimated resistance (Ω)
r_{ad}	additive resistance(Ω)
$\hat{r}_{ad}$	estimated additive resistance (Ω)
R_0	resistance of BCP at DC (Ω)
R_b	bulk resistance (Ω)
R_{gb}	grain boundaries electrolyte (Ω)
$R_{ch.t.}$	charge transfer resistance (Ω)
SOFC	solid oxide fuel cell
PS	plasma spray
SEM	scanning electron microscopy
T	time-constant (s)
$\hat{T}$	estimated time-constant (s)
TC	tape casting
T_f	period of sinusoidal signal (s^{-1})
U	voltage (V)
YDC15	$(Ce_{0.85}Y_{0.15}O_{1.925})$
Z'_i	measured real component of the impedance (Ω)
Z'_{AS}	recalculated (for elimination the effect of the electrode surface) real component of the impedance ($\Omega\,cm^2$)
Z''_I	measured imaginary component of the impedance (Ω)
Z''_{AS}	recalculated (for elimination the effect of the electrode surface) imaginary component of the impedance ($\Omega\,cm^2$)
Z_{BCP}	bounded constant phase element impedance (Ω)
ΔG	Gibbs energy (J)
$\hat{\delta}_{\hat{P}_{LOM}}$	derivative function of the LOM parameters' estimates ($d\lg\hat{P}_{LOMi}/d\lg\omega$) in secondary DIA
$\hat{\delta}_{r_{ad}}$	derivative function of $\hat{r}_{ad}$ ($d\lg\hat{r}_{ad}/d\lg\omega$) in secondary DIA
Φ	function
ρ	resistivity (Ω cm)
ω_i	angular frequency ($\omega = 2\pi f$) (s^{-1})

References

[1] S. Thorel, A. Chesnaud, M. Viviani, A. Barbucci, S. Presto, P. Piccardo, Z. Ilhan, D. E. Vladikova, Z. Stoynov, in S.C. Singhal, H. Yokokawa (Eds.), Solid Oxide Fuel Cells 11 (SOFCXI), The Electrochemical Society Proceedings Series, ECS Transactions, Vol. 25 (2), Pennington, NJ (2009) 753.
[2] S. Presto, A.Barbucci, M.Viviani, Z.Ilhan, S.A.Ansar, D. Soysal, A. Thorel, J. Abreu, A. Chesnaud, T. Politova, K. Przybylski, J. Prazuch, Z. Zhao, D. Vladikova, Z. Stoynov, in S.C. Singhal, H. Yokokawa (Eds.), Solid Oxide Fuel Cells (SOFCXI), The Electrochemical Society Proceedings Series, Pennington, NJ (2009) 773.
[3] www.ideal-cell.eu.
[4] Patent N° 0550696000, March 17th, 2005, Cellule de pile a combustible haute temperature a conduction mixte anionique et protonique, International extension in 2006.
[5] Z. Stoynov, D. Vladkova, Differential Impedance Analysis, Marin Drinov Academic Publishing House, Sofia, 2005.
[6] D. Vladikova, Z. Stoynov, G. Raikova, in: Z. Stoynov, D. Vladikova (Eds.), Portable and Emergency Energy Sources, Marin Drinov Academic Publishing House, Sofia, 2006, p. 383.
[7] Z. Stoynov, D. Vladikova, in: U. Garche (Ed.), Encyclopedia of Electrochemical Power Sources, Elsevier, 2009, p. 632.
[8] D. Vladikova, P. Zoltowski, E. Makowska, Z. Stoynov, Electrochim. Acta 47 (2002) 2943.
[9] D. Vladikova, Z. Stoynov, J. Electroanal. Chem. 572 (2004) 377.
[10] D. Vladikova, A. Kilner, S.J. Skinner, G. Raikova, Z. Stoynov, Electrochim. Acta 51 (2006) 1611.
[11] A. Barbucci, M. Viviani, P. Carpanese, D. Vladikova, Z. Stoynov, Electrochim. Acta 51 (2006) 1641.
[12] D.E. Vladikova, Z.B. Stoynov, A. Barbucci, M. Viviani, P. Carpanese, J.A. Kilner, S.J. Skinner, R. Rudkin, Electrochim. Acta 53 (2008) 7491.
[13] D. Vladikova, Z. Stoynov, A. Barbucci, M. Viviani, P. Carpanese, G. Raikova, in: L. Mitoseriu (Ed.), New Developments in Advanced Functional Ceramics, Transworld Research Network, India, 2007, p. 457.
[14] N. Bonanos, B.C.H. Steele, E.P. Butler in, E. Barsoukov, J. Ross Macdonald (Eds.), Impedance Spectroscopy, John Willey, Sons Inc., Hoboken, NJ, 2005, p. 205.
[15] J.-S. Lee, T.-J. Chung, D.-Y. Kim, Solid State Ionics 136–137 (2000) 39.
[16] J. Fleig, J. Maier, J. Am. Ceram. Soc. 82 (1999) 3485.
[17] X. Guo, W. Sigle, J. Fleig, J. Maier, Solid State Ionics 154–155 (2002) 555.
[18] J.W. Gibbs, Thermodynamische Studien Leipzig (1892) 376.
[19] C. Gabrielli, Identification of Electrochemical Processes by Frequency Response Analysis, Technical Report No 004, Solartron, Farnborough, Hampshire, England, 1980.
[20] Z. Stoynov, B. Savova-Stoynov, T. Kossev, J. Power Sources 30 (1990) 285.
[21] A. Chahremaninezhad, E. Asselin, D.G. Dixon, Electrochim. Acta 55 (2010) 5041.
[22] Z. Stoynov, in: C. Julien, Z. Stoynov (Eds.), Materials for Lithium-ion Batteries, Kluwer Academic Publishers, Dordrecht, 2000, p. 371.